Three-dimensional distribution of individual atoms in the channels of beryl

Check for updates

Daniel Knez [1] ✉, Christian Gspan[2], Nikola Šimić [2], Stefan Mitsche [1,2], Harald Fitzek [2], Karl Gatterer[3], Helmar Wiltsche[4], Gerald Kothleitner [1,2], Werner Grogger[1,2] & Ferdinand Hofer [1,2] ✉

Single atom detection in nanoporous materials is a significant challenge, particularly due to their sensitivity to electron irradiation. Here, natural beryl ($Be_3Al_2Si_6O_{18}$) is used as a model system to quantitatively analyse the occupancy of its atomic channels. High-angle annular dark-field imaging in a scanning transmission electron microscope is employed, revealing the presence of Cs atoms within the channels. Through statistical analysis of atomic column intensities and comparison with a series of multislice simulations, we successfully pinpoint the three-dimensional positions of individual Cs atoms. Our findings indicate a non-uniform distribution of Cs atoms in the crystal. Importantly, by extracting both the crystal thickness and atomic positions from a single high-resolution micrograph, we effectively minimize the adverse effects of beam damage. This approach offers a promising pathway for accurately determining the three-dimensional distribution of dopant atoms in various porous materials, opening new possibilities for the study and application of these technologically important materials.

The crystal structures of porous materials such as zeolites and metal-organic frameworks (MOFs) have been studied very extensively in recent years. The ability of these materials to incorporate ions, molecules and even clusters into the channels significantly affects their chemical properties, leading to numerous applications in science and technology, ranging from catalysis, gas separation and storage to pharmaceuticals. Surprisingly, very little is known about the detailed incorporation of these guest components and their interactions with the host crystal, although this would be of great importance for the further development of porous materials[1].

In several recent publications, atomically resolved scanning transmission electron microscopy (STEM) has been used to study guest components in porous materials. Depending on the use of an annular dark field (ADF) or differential phase contrast (DPC) detector, either heavy elements such as metal ions in beryl[2] or organic molecules in zeolites have been studied with DPC[1,3,4]. While these studies provide only qualitative information leaving many questions unanswered, more quantitative studies of the distribution of Pb clusters[5] or adsorbed molecules[6] in zeolites have been presented just recently.

For on-site analysis of dopant atoms in bulk crystal lattices, advanced methods for STEM investigations already exist, which even provide quantitative information by taking into account the detailed experimental conditions and the channelling of the electrons along the atomic columns[7–12]. However, for atoms or molecules on interstitial sites, such as those found in the channels of porous materials, further difficulties, such as the lack of electron probe confinement or small focal depth arise. This lack of channelling of electrons scattered by single atoms within a nanoporous geometry results in a distinct contrast formation when compared to dopants located on specific sites within the columns of crystalline materials[10,13] or the straightforward case of foreign atoms in a 2D material[14,15]. The high susceptibility of porous materials to electron beam damage poses additional challenges to high-resolution STEM analysis[16,17]. As a result, no work has been done to unambiguously determine the three-dimensional position of individual atoms in the pores or in the crystal channels.

To solve this problem, we chose the mineral beryl, ideally $Be_3Al_2Si_6O_{18}$, as a typical example of a porous material that has very well-defined channels along one crystal axis, that can be occupied by different guest components[18,19]. Beryl crystals are widely used as gemstones, but they are also the only source for beryllium extraction. In recent years, scientific interest in beryl crystals has grown due to the special properties of water molecules in the crystal channels, such as ultraconfinement[20], quantum tunnelling[21] and incipient ferroelectricity[22].

[1]Institute of Electron Microscopy and Nanoanalysis, Graz University of Technology, Steyrergasse 17, 8010 Graz, Austria. [2]Graz Centre for Electron Microscopy, Steyrergasse 17, 8010 Graz, Austria. [3]Institute of Physical and Theoretical Chemistry, Graz University of Technology, Stremayrgasse 9, 8010 Graz, Austria. [4]Institute of Analytical Chemistry and Food Chemistry, Graz University of Technology, Stremayrgasse 9, 8010 Graz, Austria. ✉e-mail: knez@tugraz.at; ferdinand.hofer@felmi-zfe.at

In this paper, we present a methodology to identify and localise individual Cs atoms in the channels of a beryl crystal in three dimensions, harnessing high-resolution STEM combined with statistical data analysis and modelling. We support our findings by plasma optical emission spectroscopy (ICP-OES), scanning electron microscopy (SEM) with energy- and wavelength-dispersive X-ray spectroscopy (EDS, WDS), ultraviolet–visible spectroscopy (UV-Vis) and Raman spectroscopy.

Results and discussion
The beryl structure
Beryl has a crystal structure of space group P6/mcc, which has been refined several times by X-ray and neutron diffraction[23–25]. The structure of the cyclosilicate consists of stacked six-membered rings of SiO_4 tetrahedra connected by BeO_4 tetrahedra and AlO_6 octahedra, forming a framework with channels parallel to the c-axis. The channels are not uniform in diameter but instead consist of cavities (2a sites) with a diameter of 0.5 nm separated by constrictions in the plane of the Si_6O_{18} ring with a diameter of 0.28 nm (2b sites)[24]. Figure 1b shows a ball-stick model of the structure and the location of the two cavity sites.

In natural beryl, a variety of foreign species can be incorporated into the channels of the lattice. In the latter atoms occupy octahedral and tetrahedral lattice sites, especially Li^+, Mg^{2+}, Ca^{2+} and transition metal ions such as Sc^{3+}, V^{3+}, Cr^{3+} and Mn^{2+}. Fe^{2+} and Fe^{3+} ions are also common and contribute to the pale blue colour of aquamarine[18,19,26]. It has also been suggested that some of these ions may occupy interstitial lattice sites between the octahedra and tetrahedra of the crystal[18].

The channels primarily contain small molecules and alkaline elements. Molecular species such as water, carbon dioxide or nitrogen may occupy the wider parts of the channels (2a position)[26,27] alongside larger ions such as K^+ and Cs^+[28]. Smaller ions like Li^+ or Na^+ always occupy the narrow 2b sites (centres of the Si-O-rings)[27,29]. Based on a detailed analysis of the bond lengths, it has also been proposed that Ca^{2+} and Sc^{3+} ions could be present in the channels[19]. Viana et al. suggested that Fe^{2+} may be trapped in the channels of beryl, although this has not been confirmed by other studies[30].

Pre-characterisation
A pale blue-green aquamarine crystal from Minas Gerais, Brazil (Fig. 1a) was studied as a model system. To determine the crystal's composition, a cross-sectional analysis was performed using a scanning electron microscope (see Supplementary Figs. 1, 2). Energy-dispersive X-ray spectrometry (EDS) showed concentration variations of K, Cs, Sc and Fe, with the lowest concentration in the centre and a significant increase towards the edges. The SEM-EDS analysis of the central region revealed concentrations of 0.03 at% for Cs, 0.32 at% for Fe, and only about 0.02 at% for K. Sodium was not detected (refer to Supplementary Fig. 3 and Supplementary Table 1). Subsequently, the central region was selected for TEM investigation. The crystal's composition was verified by inductively coupled plasma optical emission spectroscopy (ICP-OES) in a separate section. Please refer to the Supplementary Information (Supplementary Table 2) for more information. Additionally, ICP-OES detected Li in very low concentration.

Micro-Raman spectrometry has provided evidence for the presence of water in the crystal (spectrum provided in Supplementary Fig. 4 with band assignments listed in Supplementary Table 3). It is known that water molecules occur in two forms in beryl, distinguished by the orientation of the molecule in the channel: Type I water with the H-H vector parallel to the c-axis and type II water perpendicular to it. The results indicate a higher concentration of type I water than type II water, which is consistent with the low alkali content of the beryl[26]. Type II water is typically associated with the presence of alkali elements[27,31]. The obtained result is consistent with our elemental analysis, which revealed a total alkali element content of only 0.05 at%. Supplementary Fig. 5 shows additional optical absorption spectra measured perpendicular and parallel to the c-axis of the crystal, displaying the typical Fe absorption features of aquamarine[18,27,32], such as Fe^{3+} ions on octahedral Al^{3+} sites, neighbouring Fe^{2+}- Fe^{3+} ion pairs and Fe^{2+} also on tetrahedral sites.

To summarise, the aquamarine crystal is a type of beryl with low levels of alkali elements such as Li, K and Cs, as well as low levels of Fe. It can be classified as an octahedral beryl based on crystal-chemical analysis, with Fe mainly on the octahedral Al^{3+} lattice sites[26].

Qualitative characterisation of channel species
The high-resolution STEM micrographs, depicted in Fig. 2, exhibit a single crystalline structure of high quality and confirm the presence of atomic species within several channels in both ADF and high-angle ADF (HAADF) imaging modes, along [001] crystallographic orientation.

The ADF and HAADF images were taken simultaneously at a dose rate of 3600 e⁻ Å^{-2} s^{-1}, which corresponds to a beam current of about 30 pA. Although the beam current is half of the 60 pA used in Arivazhagan's work[2], the crystal structure disappeared within a few seconds of exposure, leaving only an amorphous layer. No diffusion of the channel occupancies could be detected.

To assign the contrast in the filled channels to the species present, we run a series of multislice simulations with different occupying atoms. In order to determine the maximum contrast which can be achieved by the different atomic species in the channel a realistic geometry is set up and compared with the experimental results. Due to the sparsity of visibly occupied channels in the STEM images, together with the low concentrations of foreign elements measured by EDS, WDS and ICP-OES, we assume that each channel is occupied by a maximum of one atom. As outlined in more detail later in this work, we find that the HAADF contrast of a single interstitial atom in the channel decreases with its depth in the crystal. Therefore, in each configuration, the atoms are placed at the top of the
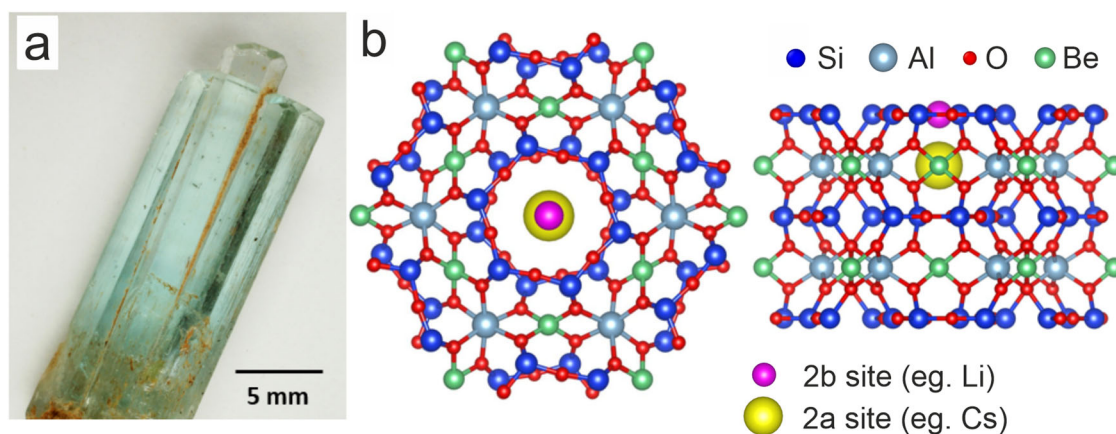
Fig. 1 | The structure of aquamarine. a Image of the crystal from Minas Gerais, Brazil; **b** Crystal structure of beryl, exemplary with a Cs atom (yellow) typically placed in the channel cavity (2a site with a diameter of 0.5 nm) and Li on the narrow 2b site (diameter 0.28 nm); top view and side view of the structure.
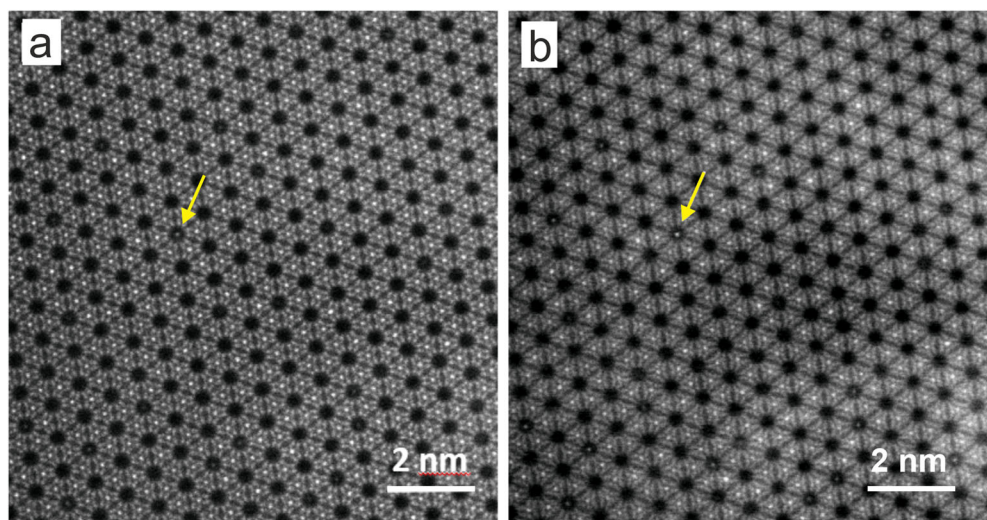
Fig. 2 | High-resolution STEM image of aquamarine viewed along the [001] direction. a HAADF and **b** ADF image, respectively. Several bright spots are visible within the channels. The arrow exemplary indicates a bright spot.
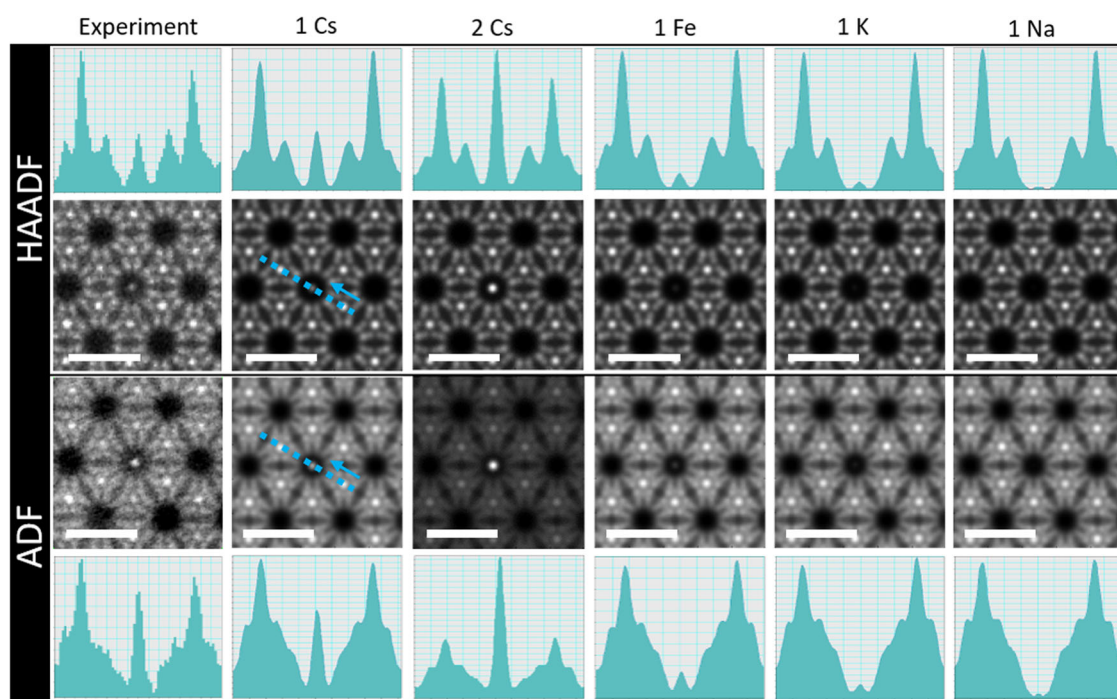
Fig. 3 | Contrast dependent on channel species. Qualitative comparison of experimental STEM images of the brightest channel occupant to multislice simulations with QSTEM viewed along the [001] direction, with various possible dopants: 1 Cs atom, 2 Cs atoms, 1 Fe atom, 1 K atom, 1 Na atom in the channel position Z = 0 for a specimen thickness of 10 nm. The position of the intensity profile is indicated by a blue dotted line and is the same for every image. The arrow indicates the direction of the profile. Scale bars are 1 nm.

channel in order to maximise the contrast. It has also been shown that the visibility of a single atom decreases with the thickness of the crystal[33,34]. The thickness of the crystal was set to 10 nm for this series, which is a realistic estimate for the lowest experimentally obtainable crystal thickness for this material. Figure 3 presents the results of the calculations in direct comparison with the corresponding experimental data, including intensity line profiles for better visualisation. A channel with an exceptionally high brightness, denoted by an arrow in Fig. 2, has been selected for comparison.

The results indicate that in our simulated scenario, which represents the case with the maximum achievable contrast of an atom within the channel, the lower Z elements Na, K and Fe are almost invisible. Although these species are expected to be present in the channels, their contribution to the HAADF contrast of the filled channels will be negligible compared to the Cs ions. This is especially true for higher sample thickness values and atom positions deeper in the crystal. Only the Cs ions with the highest atomic number Z provides a comparable contrast, leading to the conclusion that this bright channel is likely filled with at least one, or possibly two Cs ions.

To investigate the correlation between the contrast of a single Cs atom positioned near the crystal surface and the thickness, a new set of simulations was conducted. The thickness was varied up to 30.5 nm (33 unit cells). Figure 4 displays a comparison of the ADF and HAADF contrast at different thickness values with the experimental image already shown in Fig. 3 (indicated by arrows in Fig. 2). We see that the contrast of a heavy atom like Cs quickly vanishes with increasing sample thickness, underlining the
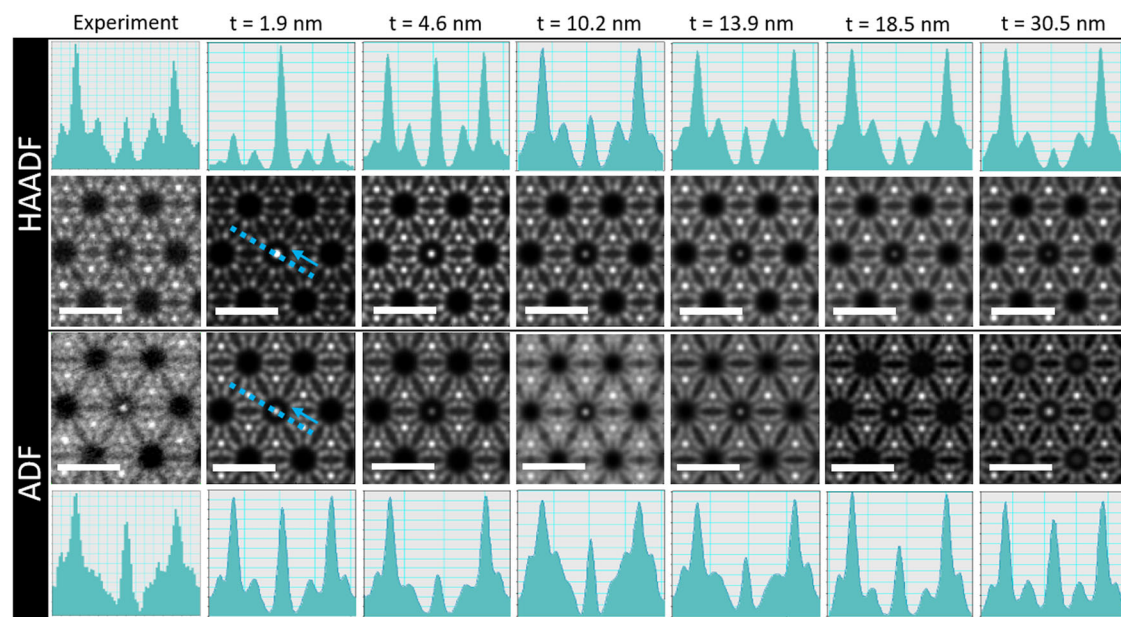
Fig. 4 | Contrast dependent on crystal thickness. Qualitative comparison of experimental STEM images of the bright channel occupant indicated in Fig. 2 to multislice simulations with QSTEM viewed along the [001] direction; with the assumption of one Cs ion in the top position t = 0 and for a specimen thickness range from 1.9 to 30.5 nm. The position of the intensity profile is indicated by a blue dotted line and is the same for every image. The arrow indicates the direction of the profile. Scale bars are 1 nm.

importance of low sample thickness for single atom analysis[34,35]. The ADF signal is particularly effective in highlighting individual channel atoms, resulting in improved identification of filled channels. However, interpreting this signal quantitatively can be challenging due to its coherent nature. It is important to note that at higher thickness values, an additional contrast starts to appear within the empty channels in the ADF images, possibly caused by electron channelling effects and the limited depth of focus of the convergent beam, which may be mistaken for filled channels. A comparable effect is also noticeable in the HAADF signal, albeit to a much lesser degree (see Supplementary Fig. 6).

The results of our qualitative analysis indicate that only Cs ions, and not lighter alkali ions can be detected in the channels of a beryl crystal with a thickness greater than 10 nm using STEM-HAADF imaging. In a previous study by ref. [2], a 40 nm thick beryl crystal of the heliodor variety was studied using STEM-HAADF. Arivazhagan et al. concluded that Fe ions also occupy the channels, as suggested by Viana et al. using optical absorption and Mössbauer spectroscopy[30]. However, the concentration of Fe ions in the channels may be too low to be detected by optical absorption and Mössbauer spectroscopy. Additionally, previous research has shown that Fe ions are only incorporated into the crystal lattice through substitution[18,19,36]. Our evaluations also suggest that the sample thickness of 40 nm is too high to detect lighter elements than Cs. We conclude that Arivazhagan et al. detected Cs ions, which are more abundant in their heliodor crystals than in ours, rather than Fe.

Quantitative analysis

According to our analysis in Figs. 3, 4, the contrast of individual Cs atoms is strongly dependent on the local thickness of the crystal, which must therefore be known for a quantitative analysis. However, determining an accurate thickness value from exactly the same area used for imaging is challenging due to the beam sensitivity of the material. Conventional thickness measurement techniques such as position-averaged convergent beam electron diffraction (PACBED) or electron energy-loss spectrometry (EELS) are unsuitable in our case as they induce beam-induced amorphization, leading to a significant alteration in the thickness of the crystalline part[37–40]. In addition, the image acquisition itself introduces additional amorphization, further changing the crystalline thickness simultaneously in the imaged region.

Here we take a different approach and determine the thickness directly from the same HAADF image that is also used for quantification, by comparing the intensity ratio of the Al and Si atomic columns with a series of multislice contrast simulations. For the quantitative analysis, a homogeneous region containing six filled channels was selected from a HAADF micrograph (depicted in Fig. 5a, b). The positions of the atomic columns for Si, Al and the channels and their corresponding intensities are determined as described in the Methods section. This procedure gives an intensity value for each of the visible atomic columns, as shown in Fig. 5c. From the histogram of the column intensities shown in Fig. 5d, we can clearly distinguish the different atomic columns. By performing a classification based on a four-component Gaussian mixture model, we separate the partially overlapping contributions and calculate their mean intensities[11]. After subtracting the vacuum intensity (of $7.8 \cdot 10^4$ counts), we calculate the Al/Si ratio from the mean intensity values, which gives a value of 1.31. Using ratios instead of absolute values has two major advantages: On the one hand, multiplicative experimental uncertainties cancel each other out, thereby increasing the accuracy of the results[41]. On the other hand, our simulations (see Supplementary Fig. 7) show that the contribution of an amorphous surface layer to the intensities can be neglected to some extent in a ratio-based analysis, inspired by an idea of ref. [42]. To perform the comparative simulations, a beryl crystal model with a maximum thickness of 38 nm and a Cs atom at the top (as shown in Fig. 1b) is constructed. To account for the Fe occupation on the Al sites, 4.4% of the Al atoms were randomly replaced by Fe, corresponding to the total Fe content in the crystal as determined by EDS and ICP-OES analysis. To account for the statistical intensity variations caused by different depth distributions of the Fe atoms within the Al channels, the intensities are averaged over three multislice runs with different randomised Fe positions. The resulting Al/Si ratio is plotted as a function of the thickness for each slice in Fig. 5e. Comparison with the experimental value of 1.31 gives a thickness value of about 18 ± 3 nm in the analysed region. The margin of error is derived from the deviation of the Al/Si intensity ratio with increasing amorphous layers, which is explained in more detail in the Supporting Information (see Supplementary Note 5).

This result has been double-checked by STEM-EELS obtained from a nearby region, which gives thickness values in the range between 26 to 45 nm ($t/\lambda = 0.14$–0.25 where λ is the inelastic mean free path length and $\lambda = 183$ nm
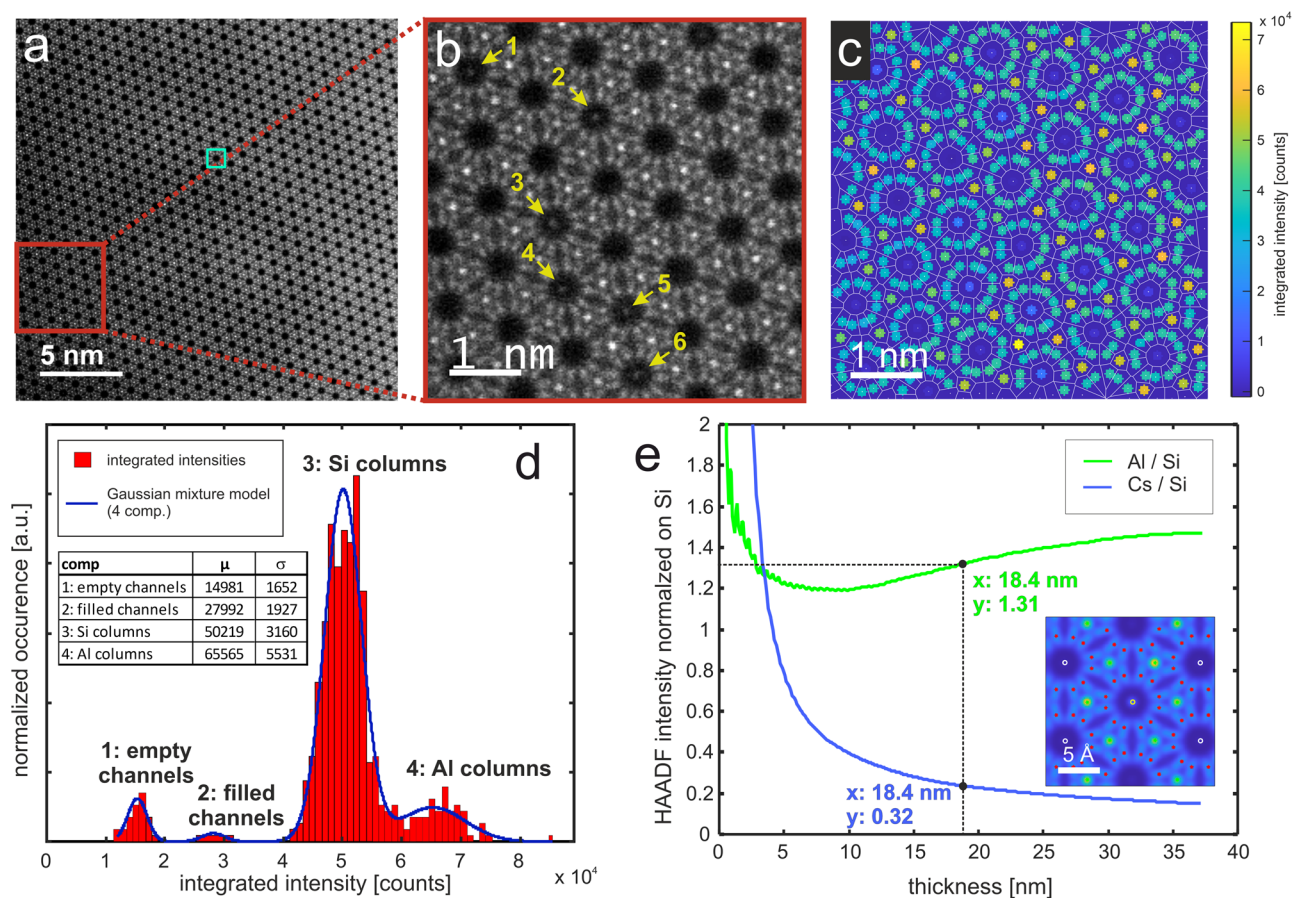
Fig. 5 | Quantitative interpretations of the HAADF signal. a Overview STEM-HAADF micrograph; **b** Magnified region highlighted in (**a**) containing six filled channels; **c** Quantitative analysis of the atomic columns with Voronoi tessellation and areal integration; **d** histogram of the intensities determined in **c**. The different contributions and their mean values are determined with a four-component Gaussian mixture model with the corresponding Gaussian parameters µ (mean) and σ (standard deviation) given in the inset table. **e** Al/Si and Cs/Si intensity ratios over thickness obtained from multislice simulation series with one Cs atom at the top position in the channel.

for the material and experimental conditions according to the approximation by Iakoubovskii et al. (2008) with density $\rho = 2640\,\mathrm{kg\,m^{-3}}$)[39,43,44]. Note that this includes the amorphous layers that are inevitably introduced by beam damage and ion beam milling during sample preparation on both surfaces of the crystal. For beryl, which is a poor electrical conductor, the dominant damage mechanism in the electron beam is radiolysis[45]. The finely focused beam in the STEM further induces strong local fields in insulating materials, which enhances permanent atomic displacements, particularly in porous materials[16,46]. Both effects lead to rapid amorphization of the crystal. One should be aware that the surface amorphization is likely to have a different inelastic mean free path length than the crystalline sample and significant deviations have been reported for some materials and experimental settings[47,48]. Accordingly, the EELS result represents an upper limit and the crystalline part of the sample must be thinner. This is in good agreement with the value obtained by our method, taking into account the sensitivity of the material and the additional amorphization due to beam damage during sample preparation and data acquisition[45,49], and also aligns with PACBED measurements obtained from other experiments with beryl[37]. The simulated Cs/Si ratio at the measured crystal thickness gives a value of 0.32, which represents an estimate for the maximum value that is expected from a single Cs atom at the top position of the crystal with a thickness of 18 nm.

With the thickness value now determined, another series of multislice simulations is performed at constant thickness but with varying z-positions of the Cs atoms in the channel. To account for the background intensity within the channels, the empty channel intensity is subtracted from the filled channels before calculating the ratios. The resulting Cs/Si ratios are shown in blue in Fig. 6 as a function of the z-position

(measured from the top of the crystal). The curve shows a monotonic decrease of the ratio with the Cs z-position, which can be used to determine the positions of the atoms from the experimental data for the six channels identified in Fig. 5b.

Our simulation data shows that the presence of amorphous layers has a different impact on the detected HAADF intensity at the channel positions compared to the atomic columns (see Fig. S7 in the Supporting Information). This discrepancy in scattering behaviour is attributed to the distinct atomic geometry, which requires the introduction of a correction factor for the measured intensities[42]. To this end, we are using the brightest Cs ion as a reference, assuming that it occupies the top position of the crystal. As shown in the simulations above, in such a case, a Cs/Si intensity ratio of 0.32 is determined. To obtain the same Cs/Si ratio for the brightest Cs atom in our experiment, this ratio needs to be adjusted by a factor of 0.97, which is then used to correct the remaining Cs/Si ratios. After subtraction of the mean empty channel/Si ratio (0.3) for each occupied channel, we determine the resulting z-positions for each Cs/Si value through linear interpolation from the simulated values. The obtained positions are indicated by red dots in Fig. 6 and align well with the images in Fig. 4 and the simulated and experimental images presented in Fig. 6.

Uncertainties of the determined depth values are introduced by noise and scanning artefacts. We estimated their impact by fitting two-dimensional Gaussian functions to the individual Cs positions and calculating the root mean square (RMS) of the per-pixel differences between the fit and the experiment. We find errors of ~5% of the determined intensity values which corresponds to the error bars provided in Fig. 6. Thus, we should, in principle, be able to distinguish two possible Cs positions,
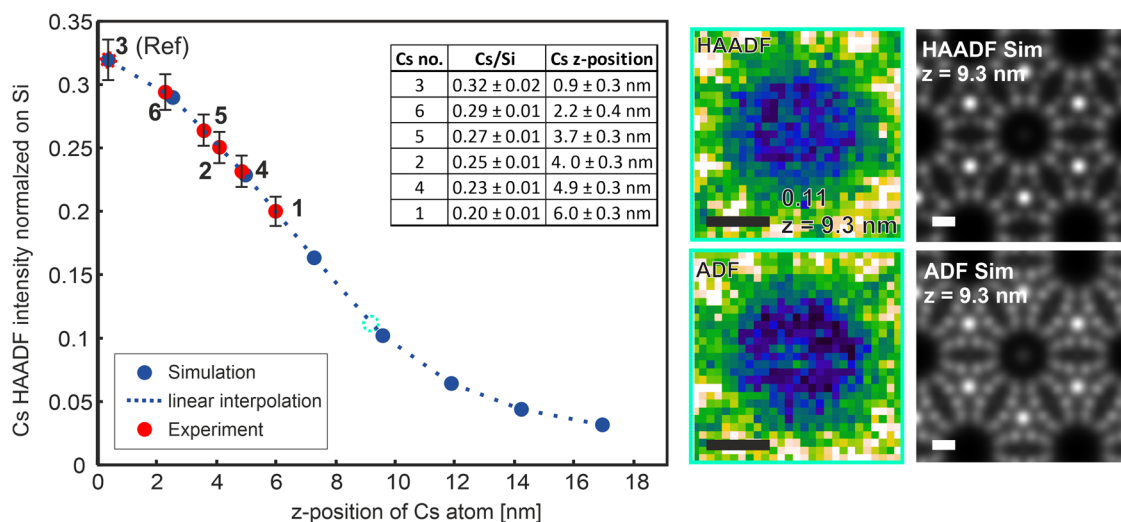
Fig. 6 | Measure the depth of the Cs atoms. Cs/Si intensity ratios obtained from varying Cs z-positions in the channel, blue dots are extracted from simulations at the measured crystal thickness and red dots correspond to the experimental data with according to numbering shown in Fig. 5b with their ratio and position values given in the inset table. The images demonstrate the experimental detection limit of a single Cs atom in the channel, identified in the region highlighted in Fig. 5a and a comparison with a simulated image with a Cs atom placed at the determined depth. Scale bars are 2 Å.

considering the distance of 0.93 nm between two $2a$ sites in the channel (see Fig. 1).

Strikingly, all of the calculated values are found in the upper half of the sample. The reason for this becomes clear when we determine the depth for the filled channel with the weakest contrast found in Fig. 5a (highlighted by a cyan square), being only slightly above the amorphous intensity level. For this channel, the ADF contrast was used to visually identify the channel, as the HAADF contrast is very weak at this position. A comparison of both images together with the corresponding simulated images with a Cs atom placed at a depth of 9.3 nm and a total thickness of 18 nm is shown in the images in Fig. 6. This gives a rough estimate for the lower limit for the detection of filled channels in the experimental images is determined. Single Cs atoms at greater depths will be invisible under the given experimental conditions and sample thickness. Notably, Cs atoms are not distributed homogenously in the crystal. Several regions are found, as shown in Fig. 5b, containing several visible Cs atoms within an area of approximately 4×4 nm² (and an estimated depth range of ~5 nm), with larger empty areas in between.

From the numbers obtained, we can now estimate the local Cs concentration for the whole area imaged in Fig. 5a. The image contains 747 channels, from which 64 were identified as filled from the ADF image. Considering that each unit cell can host one Cs atom, a local concentration of 0.03 at% is calculated, assuming that each channel is filled with a maximum of one Cs atom and that about half of them are invisible due to their depth in the crystal. This value corresponds to the experimental value from the SEM-EDS analysis (0.03 at%).

It should be noted that the quantification could also be affected by the defocus. To minimise this influence, we set the defocus in the HAADF images to maximum contrast, corresponding to a focal point at the top of the crystal. The depth distribution of the Cs atoms is further limited by the vertical resolution, which can reach up to a few nanometres[49]. However, for isolated objects, such as single heavy atoms, the precision is much better (well below 1 nm), as demonstrated by ref. [50].

It should furthermore be noted that we cannot directly account for the intensity contributions of light element species within the channels. Considering the extremely small contributions of light elements with low concentration to the detected HAADF signal, it is reasonable to conclude that their impact on our results is negligible. Another source of error might arise from two Cs atoms within the same channel, if their combined intensity falls below the maximum intensity ratio for a single Cs atom, as determined from the simulations. However, such cases are relatively rare due to the low

concentrations of Cs in the crystal. For the given Cs concentration and crystal thickness, on average less than 10% of all channels contain a single Cs atom. Accordingly, the probability that a channel is occupied by two Cs atoms is less than 1%.

While the proposed method is suitable for quantifying heavy elements such as Cs in porous materials, we cannot easily distinguish between the different atomic species based on HAADF images alone. Initial experiments with integrated differential phase contrast (iDPC) measurements show that also lighter elements can be detected in addition to Cs atoms, but quantification is even more challenging in this case[51]. Another limitation is the modelling of the amorphous layer, which also affects HAADF intensities, especially in porous materials. To establish a more quantitative model of surface amorphization, it would be necessary to obtain data regarding its thickness, composition, and atomic displacement factors. These details would need to be extracted from dedicated experiments combined with sophisticated molecular dynamic modelling of amorphization and atomic vibrations[42]. This is a complex challenge and will be the subject of future research. Furthermore, combining various contrast mechanisms with high-sensitivity EELS and EDS spectroscopy data may provide additional opportunities for quantitative assessment of different species in crystal channels[52,53]. However, this approach also poses significant challenges due to its higher dose requirements. Detecting the EDS signal of a single atom in a sample is difficult due to the limited detection solid angles and the absorption of the X-rays emitted by the single atom within the crystal. In contrast, EELS is better suited for this purpose. However, detecting the EELS or EDS signal from single atoms requires significantly higher doses due to the lower scattering cross-section of inelastic scattering compared to the cross-section for STEM-HAADF imaging. Experiments at cryogenic temperatures would certainly be helpful to reduce beam damage effects to allow to detect lighter elements and to use spectroscopic techniques at atomic resolution. With the further development of high-speed and high-sensitivity detectors, ptychography-based techniques might become suitable for detecting and localising single interstitial atoms also from lighter elements in three dimensions within beam-sensitive, porous materials[10].

In summary, our quantitative evaluation of high-resolution HAADF micrographs clearly shows that only Cs atoms, but not lighter atoms (alkaline elements or transmission metals Sc or Fe), can be detected in the channels of beryl, contradicting previous reports in the literature. By developing our approach based on a statistical analysis of HAADF intensity ratios and comparative multislice simulations, we are able to extract local sample thickness information and localise individual Cs atoms in three

dimensions from a single micrograph. It will be the subject of future work to clarify the question of the role of Cs atoms in the channels, which act as charge balancers mediating intervalence charge transfer between adjacent Fe atoms on lattice sites, leading to the typical aquamarine colour[18]. Our results demonstrate that electron microscopy methods can be used very successfully for the quantitative analysis of individual atoms in nanoporous materials, which generally exhibit high beam sensitivity. More generally, our work may be instructive for future efforts to elucidate the spatial distribution of guest species incorporated into other nonporous material systems.

Methods
Material
The aquamarine crystal has a pale blue colour with a green tinge and comes from Minas Gerais in Brazil. The natural crystal is of hydrothermal origin; it is covered with an Fe-rich mineral.

Sample preparation
The crystal was cut perpendicular to the c-axis and carefully polished. For the optical measurements (UV-Vis), a thin transparent slice was used. The sample for TEM measurements was thinned using a dimple grinder followed by Ar^+ ion milling (PIPS from Gatan Inc., USA) until electron transparency was achieved. For the final cleaning step, we used a Nanomill 1040 system (Fischione Inc. USA).

STEM-HAADF investigation
High-resolution HAADF STEM investigations were carried out on a probe-corrected FEI Titan[3] (Thermo Fisher Scientific, Eindhoven) operated at 300 kV with a field emission source (X-FEG) at a convergence angle of 19.6 mrad. The microscope is equipped with an electron energy-loss filter (GIF Quantum, Gatan) and a Super-X EDS detector (Thermo Fisher, Eindhoven). The angular range of the HAADF detector (Fischione) is 62.2 to 214.0 mrad and that of the ADF detector is 19.5 to 62.0 mrad (Gatan), both corresponding to a nominal camera length of 91 mm.

The brightness and contrast levels were set low enough to ensure that the detectors are not saturated and kept constant for all experiments.

Quantitative analysis of both the HAADF micrographs and multislice simulations was performed using a custom code written in MathWorks Inc. Matlab (version R2020)[54]. To this end, the positions of the atomic columns are determined by searching for local intensity maxima. For the channel's local maxima for the inversed image were determined. For the experimental data, a spatial average filter was applied to reduce the influence of noise on the performance of the peak-finding algorithm. The obtained peak positions are subsequently used as a basis for Voronoi tessellation. Based on the resulting cells, we determine the absolute intensity from the unfiltered image, integrated over a radius of three pixels (or 0.067 nm) corresponding to each atomic column. The integrated column intensity is a robust measurement as it has been shown to be insensitive to probe shape and defocusing[55].

Image simulation
The STEM-HAADF and ADF images in Figs. 3, 4 were simulated with the programme QSTEM V2.4 (written by C.K. Koch at the Arizona State University, Tempe, USA)[56]. The simulations for the quantitative analysis of the HAADF images were performed with Dr. Probe (developed by Juri Barthel at Forschungszentrum Jülich/Germany)[57]. The full-width at half maximum of the probe was set to 0.08 nm. To account for thermal diffuse scattering, five runs were calculated for the qualitative QSTEM simulations (Figs. 3, 4), while 20 runs were performed for the quantitative simulations in Dr. Probe, with atomic displacement factors from ref. [23].

Additional characterisation methods
The chemical analysis was performed by optical emission spectrometry with an inductively coupled plasma (ICP-OES) (Spectro Ciros Vision EOP, Spectro, Kleve, DE) with axial plasma observation. To this end part of the

crystal was pulverised in a ball mill and treated with microwave-based acid digestion Multiwave 3000 with XF100-8 rotor (Anton Paar) at 60 bar.

The cross-section of the crystal was examined with a scanning electron microscope (SEM, Zeiss Ultra 55) equipped with a field emission gun, an angle-sensitive backscatter electron detector (AsB), an energy-dispersive X-ray spectrometer (Genesis, EDAX LLC) and a wavelength-dispersive X-ray spectrometer (Lamba Spec, EDAX). The acceleration voltage of the SEM was set to 15 kV.

Raman microscopy measurements were performed with a Horiba Jobin Yvon LabRam 800 HR spectrometer equipped with a 1024×256 CCD (Peltier-cooled) and an Olympus BX41 microscope. All measurements were done using a laser wavelength of 532 nm (50 mW), an x50 Olympus LMPlanFLN (N.A. 0.5) objective.

Transmission spectra in the UV-Vis range were obtained from a 1 mm thick slice of the crystal cut perpendicular to the c-axis. The crystal was placed in the sample beam of a Lambda 950 double-beam spectrometer (Perkin Elmer) with the reference beam path being empty.

Data availability
Details on the sample characteristics and composition are included in the SI Appendix. Additional simulation data is also given in the SI Appendix. Further data supporting the findings of this study are available from the authors upon reasonable request.

Code availability
Custom Matlab code used for data analysis is available from the authors on reasonable request.

References
1. Shen, B. et al. Atomic imaging of zeolite-confined single molecules by electron microscopy. *Nature*. https://doi.org/10.1038/s41586-022-04876-x (2022).
2. Arivazhagan, V., Schmitz, F. D., Vullum, P. E., van Helvoort, A. T. J. & Holst, B. Atomic resolution imaging of beryl: an investigation of the nano-channel occupation. *J. Microsc.* **265**, 245–250 (2017).
3. Liu, L., Zhang, D., Zhu, Y. & Han, Y. Bulk and local structures of metal–organic frameworks unravelled by high-resolution electron microscopy. *Commun. Chem.* https://doi.org/10.1038/s42004-020-00361-6 (2020).
4. Shen, B., Chen, X., Shen, K., Xiong, H. & Wei, F. Imaging the node-linker coordination in the bulk and local structures of metal-organic frameworks. *Nat. Commun.* **11**, 2692 (2020).
5. Fatermans, J. et al. Atomic-scale detection of individual lead clusters confined in Linde Type A zeolites. *Nanoscale* **14**, 9323–9330 (2022).
6. Zhang, H. et al. Three-dimensional inhomogeneity of zeolite structure and composition revealed by electron ptychography. *Science* **380**, 633–638 (2023).
7. Voyles, P. M., Muller, D. A., Grazul, J. L., Citrin, P. H. & Gossmann, H.-J. L. Atomic-scale imaging of individual dopant atoms and clusters in highly n-type bulk Si. *Nature* **416**, 826–829 (2002).
8. Hwang, J., Zhang, J. Y., D'Alfonso, A. J., Allen, L. J. & Stemmer, S. Three-dimensional imaging of individual dopant atoms in SrTiO3. *Phys. Rev. Lett.* **111**, 266101 (2013).
9. Varela, M. et al. Spectroscopic imaging of single atoms within a bulk solid. *Phys. Rev. Lett*. https://doi.org/10.1103/PhysRevLett.92.095502 (2004).
10. Chen, Z. et al. Electron ptychography achieves atomic-resolution limits set by lattice vibrations. *Science* **372**, 826–831 (2021).
11. van Aert, S., Batenburg, K. J., Rossell, M. D., Erni, R. & van Tendeloo, G. Three-dimensional atomic imaging of crystalline nanoparticles. *Nature* **470**, 374–377 (2011).

12. van den Bos, K. H. W. et al. The atomic lensing model: new opportunities for atom-by-atom metrology of heterogeneous nanomaterials. *Ultramicroscopy* **203**, 155–162 (2019).

13. Kimoto, K., Xie, R.-J., Matsui, Y., Ishizuka, K. & Hirosaki, N. Direct observation of single dopant atom in light-emitting phosphor of β-SiAlON:Eu2+. *Appl. Phys. Lett.* **94**, 41908 (2009).

14. Susi, T. et al. Single-atom spectroscopy of phosphorus dopants implanted into graphene. *2D Mater.* **4**, 21013 (2017).

15. Hardcastle, T. P. et al. Mobile metal adatoms on single layer, bilayer, and trilayer graphene: An ab initio DFT study with van der Waals corrections correlated with electron microscopy data. *Phys. Rev. B.* https://doi.org/10.1103/PhysRevB.87.195430 (2013).

16. Girelli Consolaro, V., Rouchon, V. & Ersen, O. Electron beam damages in zeolites: a review. *Micropor. Mesopor. Mater.* **364**, 112835 (2024).

17. Knez, D. et al. Transformation dynamics of Ni clusters into NiO rings under electron beam irradiation. *Ultramicroscopy* **176**, 105–111 (2017).

18. Andersson, L. O. Comments on beryl colors and on other observations regarding iron-containing beryls. *Canad. Mineral.* **57**, 551–566 (2019).

19. Bačík, P. & Fridrichová. J. The site occupancy assessment in beryl based on bond-length constraints. *Minerals* **9**, 641 (2019).

20. Anovitz, L. M., Mamontov, E., ben Ishai, P. & Kolesnikov, A. I. Anisotropic dynamics of water ultraconfined in macroscopically oriented channels of single-crystal beryl: a multifrequency analysis. *Phys. Rev. E Stat. Nonlinear Soft Matter Phys.* **88**, 52306 (2013).

21. Kolesnikov, A. I. et al. Quantum tunneling of water in beryl: a new state of the water molecule. *Phys. Rev. Lett.* **116**, 167802 (2016).

22. Gorshunov, B. P. et al. Incipient ferroelectricity of water molecules confined to nano-channels of beryl. *Nat. Commun.* **7**, 12842 (2016).

23. Artioli, G., Rinaldi, R., Stahl, K. & Zanazzi, P. F. Structure refinements of beryl by single-crystal neutron and X-ray diffraction. *Am. Mineral.* **78**, 762–768 (1993).

24. Gibbs, G. V., Breck, D. W. & Meagher, E. P. Structural refinement of hydrous and anhydrous synthetic beryl, Al2(Be3Si6)O18 and emerald, Al1.9Cr0.1 (Be3Si6)O18. *Lithos* **1**, 275–285 (1968).

25. Bragg, L. W. & West, J. The Structure of Beryl, Be3Al2Si6O_18. *Proc. R. Soc. Lond. Ser. A Contain. Pap. Math. Phys. Character* **111**, 691–714 (1926).

26. Aurisicchio, C., Fioravanti, G., Grubessi, O. & Zanazzi, P. F. Reappraisal of the crystal chemistry of beryl. *Am. Mineral.* **73**, 826–837 (1988).

27. Wood, D. L. & Nassau, K. The characterization of beryl and emerald by visible and infrared absorption spectroscopy. *Am. Mineral.* **53**, 777–800 (1968).

28. Hawthorne, F. C. & Cerny, P. The alkali-metal positions in Cs-Li beryl. *Canad. Mineral.* **15**, 414–421 (1977).

29. Aines, R. D. & Rossman, G. R. The high temperature behavior of water and carbon dioxide in cordierite and beryl. *Am. Mineral.* **69**, 319–327 (1984).

30. Viana, R. R., Jordt-Evangelista, H., Da Costa, G. M. & Stern, W. B. Characterization of beryl (aquamarine variety) from pegmatites of Minas Gerais, Brazil. *Phys. Chem. Miner.* **29**, 668–679 (2002).

31. Łodziński, M. et al. ICP, IR, Raman, NMR investigations of beryls from pegmatites of the Sudety Mts. *J. Mol. Struct.* **744-747**, 1005–1015 (2005).

32. Hu, Y. & Lu, R. Color characteristics of blue to yellow beryl from multiple origins. *G&G* **56**, 54–65 (2020).

33. Mittal, A. & Mkhoyan, K. A. Limits in detecting an individual dopant atom embedded in a crystal. *Ultramicroscopy* **111**, 1101–1110 (2011).

34. Voyles, P. M., Grazul, J. L. & Muller, D. A. Imaging individual atoms inside crystals with ADF-STEM. *Ultramicroscopy* **96**, 251–273 (2003).

35. Furnival, T. et al. Adatom dynamics and the surface reconstruction of Si(110) revealed using time-resolved electron microscopy. *Appl. Phys. Lett.* **113**, 183104 (2018).

36. Spinolo, G., Fontana, I. & Galli, A. Optical absorption spectra of Fe2+ and Fe3+ in beryl crystals. *Phys. Status Solidi* (b) **244**, 4660–4668 (2007).

37. Oberaigner, M. et al. Online thickness determination with position averaged convergent beam electron diffraction using convolutional neural networks. *Microsc. Microanal.* **29**, 427–436 (2023).

38. LeBeau, J. M. et al. High-angle scattering of fast electrons from crystals containing heavy elements: Simulation and experiment. *Phys. Rev. B* **79**. https://doi.org/10.1103/PhysRevB.79.214110 (2009).

39. Egerton, R. F. Electron energy-loss spectroscopy in the TEM. *Rep. Prog. Phys.* **72**, 16502 (2009).

40. Malis, T., Cheng, S. C. & Egerton, R. F. EELS log-ratio technique for specimen-thickness measurement in the TEM. *J. Electron Microsc. Tech.* **8**, 193–200 (1988).

41. Martinez, G. T. et al. Quantitative STEM normalisation: the importance of the electron flux. *Ultramicroscopy* **159P1**, 46–58 (2015).

42. Grieb, T. et al. Quantitative HAADF STEM of SiGe in presence of amorphous surface layers from FIB preparation. *Ultramicroscopy* **184**, 29–36 (2018).

43. Mitchell, D. R. G. & Schaffer, B. Scripting-customized microscopy tools for digital micrograph. *Ultramicroscopy* **103**, 319–332 (2005).

44. Iakoubovskii, K., Mitsuishi, K., Nakayama, Y. & Furuya, K. Thickness measurements with electron energy loss spectroscopy. *Microsc. Res. Tech.* **71**, 626–631 (2008).

45. Egerton, R. F., Li, P. & Malac, M. Radiation damage in the TEM and SEM. *Micron* **35**, 399–409 (2004).

46. Jiang, N. Beam damage by the induced electric field in transmission electron microscopy. *Micron* **83**, 79–92 (2016).

47. Craven, A. J., Bobynko, J., Sala, B. & MacLaren, I. Accurate measurement of absolute experimental inelastic mean free paths and EELS differential cross-sections. *Ultramicroscopy* **170**, 113–127 (2016).

48. Basha, A. et al. Elastic and inelastic mean free paths for scattering of fast electrons in thin-film oxides. *Ultramicroscopy* **240**, 113570 (2022).

49. Barna, Á., Pécz, B. & Menyhard, M. TEM sample preparation by ion milling/amorphization. *Micron* **30**, 267–276 (1999).

50. Borisevich, A. Y., Lupini, A. R. & Pennycook, S. J. Depth sectioning with the aberration-corrected scanning transmission electron microscope. *Proc. Natl Acad. Sci. USA* **103**, 3044–3048 (2006).

51. Liu, L. et al. Direct imaging of atomically dispersed molybdenum that enables location of aluminum in the framework of zeolite ZSM-5. *Angew. Chem.* **132**, 829–835 (2020).

52. Egerton, R. F. & Watanabe, M. Spatial resolution in transmission electron microscopy. *Micron* **160**, 103304 (2022).

53. Egerton, R. F. & Watanabe, M. Characterization of single-atom catalysts by EELS and EDX spectroscopy. *Ultramicroscopy* **193**, 111–117 (2018).

54. Knez, D. et al. Unveiling oxygen vacancy superstructures in reduced anatase thin films. *Nano Lett.* **20**, 6444–6451 (2020).

55. E, H. et al. Probe integrated scattering cross sections in the analysis of atomic resolution HAADF STEM images. *Ultramicroscopy* **133**, 109–119 (2013).

56. Koch, C. *Determination of Core Structure Periodicity and Point Defect Density along Dislocations*. Dissertation, Arizona State Univ. (2002).

57. Barthel, J. Dr. Probe: a software for high-resolution STEM image simulation. *Ultramicroscopy* **193**, 1–11 (2018).

Acknowledgements

Author contributions

C.G. carried out the electron microscopy experiments. D.K. performed the data analysis. N.Š. and D.K. planned and executed the multislice simulations. F.H. conceived the experiments and supervised the simulations and data analysis. H.W. conducted the ICP-OES measurements and S.M. acquired SEM micrographs and did EDS and WDS. Supporting optical spectroscopy was performed by K.G. (UV-Vis) and H.F. (Raman). G.K. and W.G. contributed to the discussion of results and to reviewing drafts. D.K. and F.H. wrote the manuscript with the contribution from all the authors.

Competing interests

The authors declare no competing interests.

Additional information

Supplementary information The online version contains supplementary material available at https://doi.org/10.1038/s43246-024-00458-8.

Correspondence and requests for materials should be addressed to Daniel Knez or Ferdinand Hofer.

Reprints and permissions information is available at http://www.nature.com/reprints

Publisher's note Springer Nature remains neutral with regard to jurisdictional claims in published maps and institutional affiliations.